2006

Optical Characterization of Electrochemically Self-Assembled Compound Semiconductor Nanowires

Sivakumar Ramanathan
Virginia Commonwealth University

School of Engineering
Virginia Commonwealth University

This is to certify that the thesis prepared by Sivakumar Ramanathan entitled OPTICAL CHARACTERIZATION OF ELECTROCHEMICALLY SELF-ASSEMBLED COMPOUND SEMICONDUCTOR NANOWIRES HAS been approved by his committee as satisfactory completion of the thesis requirement for the degree of Master of Science.

Supriyo Bandyopadhyay, Ph.D., Committee Chair, Department of Electrical and Computer Engineering and Department of Physics

---

Gregory B. Tait, Ph.D., Committee Member, Department of Electrical and Computer Engineering and Department of Physics

---

Shiv N. Khanna, Ph.D., Committee Member, Department of Physics

---

Ashok Iyer, Ph.D., Department Chair, Department of Electrical and Computer Engineering

---

L. Thomas Overby, Ph.D., Assistant Dean of Graduate Affairs, School of Engineering

---

Russell Jamison, Ph.D., Dean, School of Engineering

F. Douglas Boudinot, Ph.D., Dean, School of Graduate Studies

September 15, 2006

Dedicated

to

…… My Beloved parents

OPTICAL CHARACTERIZATION OF ELECTROCHEMICALLY SELF ASSEMBLED COMPOUND SEMICONDUCTOR NANOWIRES

A thesis submitted in partial fulfillment of the requirements for the degree of Master of Science at Virginia Commonwealth University.

by

SIVAKUMAR RAMANATHAN
B.E., University of Madras (Tamilnadu, India), 2003

Director: SUPRIYO BANDYOPADHYAY
PROFESSOR, DEPARTMENT OF ELECTRICAL AND COMPUTER ENGINEERING AND DEPARTMENT OF PHYSICS

Virginia Commonwealth University
Richmond, Virginia
September, 2006

Acknowledgement

I feel privileged to express unfeigned thanks, and gratitude to my thesis advisor Professor Supriyo Bandyopadhyay, for his constant guidance and inspiration that helped me to complete this work.

I would like to thank like Dr. John Anderson, Jarrod Edwards, and Jean Nelson for carrying out fluorescence spectroscopy measurements.

I am especially grateful to Dr. Shiv Khanna, Dr. Gregory Tait for agreeing to serve in my Master thesis committee.

I am greatly thankful to Sridhar Patibandla, Yanbin Wang for their support and constant encouragement during this work and also other members in Quantum Device Laboratory.

Table of Contents

Page

List of Tables

Page

List of Figures

Page

Abstract

OPTICAL CHARACTERIZATION OF ELECTROCHEMICALLY SELF ASSEMBLED COMPOUND SEMICONDUCTOR NANOWIRES

By Sivakumar Ramanathan

A Thesis submitted in partial fulfillment of the requirements for the degree of Master of Science at Virginia Commonwealth University.

Virginia Commonwealth University, 2006

Major Director: Dr. Supriyo Bandyopadhyay
Professor, Department of Electrical and Computer Engineering and Department of Physics

Semiconductor nanowires have attracted considerable attention as possible source for lasers and optical storage media. We report the fabrication and optical characterization of ZnO and CdS nanowires. The former are produced by electrochemical deposition of Zn inside nanoporous alumina films containing regimented arrays of 10nm, 25nm and 50 nm diameter pores, followed by room temperature chemical oxidization. Fluorescence spectroscopy shows different characteristics associated with different sample diameter. The 50 nm ZnO nanowires show an exciton recombination peak and an additional peak related to the deep trap levels. 25 nm ZnO nanowires show a only the exciton recombination peak, which is red shifted, possibly due to quantum confined Stark effect associated with built in charges in the alumina. This feature can be exploited to produce light emitting devices

whose frequency can be modulated with an external electric field. Such devices could be novel ultra-violet frequency modulators for optical communication and solar blind materials. In addition, we have investigated fluorescence spectra of 10-, 25- and 50-nm diameter CdS nanowires (relative dielectric constant = 5.4) self assembled in a porous alumina matrix (relative dielectric constant = 8-10). The spectra reveal peaks associated with free electron-hole recombination. The 10-nm wire spectra show an additional lower energy peak due to exciton recombination. In spite of dielectric de-confinement caused by the insulator having a *higher* dielectric constant than the semiconductor, the exciton binding energy increases almost 8-fold from its bulk value in the 10 nm wires. This increase is most likely due to quantum confinement accruing from the fact that the exciton Bohr radius (~5 nm) is comparable to or larger than the wire radius, especially if side depletion is taken into account. Such an increase in the binding energy could be exploited to make efficient room temperature luminescent devices in the visible range.

Keywords: Zinc oxide, quantum dots, fluorescence, quantum confined Stark effect excitons, dielectric de-confinement, binding energy

CHAPTER 1 Quantum confined Stark effect (QCSE)

In bulk semiconductors, exciton peak in the fluorescence spectra are usually observed at low temperatures due to small binding energy of excitons. In most cases, the exciton resonance peak merges with band-band transitions or is thermally ionized. In the last decade, fabrication of heterostructures has given rise to many interesting results associated with exciton transitions. Carrier confinement squeezes electrons and holes together which increases the Coulomb interaction between them, which, in turn increases the binding energy. Extremely sharp resonances can be observed at room temperatures and above in heterostructures. Moreover, the energy or strength of these resonances can be controlled easily by simple electric field or optics. There are several different methods to achieve modulation of optical properties, but only electric field induced modulation can be used for high-speed modulation of optical signals for optical communication purpose.

Let us focus our attention on emission or absorption spectra in nanowires in the presence of electric field. If an electric field is present in the longitudinal direction, we get excitonic transition similar to the bulk semiconductor and the exciton peak disappears at very low applied field. The field can ionize the excitons since there is no confinement in the longitudinal direction. A transverse electric field cannot ionize excitons because of carrier confinement in the transverse direction. It is possible that exciton transitions can even persist up to electric field greater than the ionization field. This effect is called as "*Quantum confined Stark effect*" (QCSE). There are many factors associated with QCSE.

First, the inter-band energy separation changes, as the electric field pushes the electron and hole wavefunctions in opposite directions resulting in overall net reduction in the energy of both electrons and holes. This induces a red shift in the exciton resonance energy. It also reduces the binding energy of the exciton, since the overlap between the electron and hole wavefunctions is decreased. The figure below shows the effect of an electric field, which skews the electrons and hole wavefunctions.

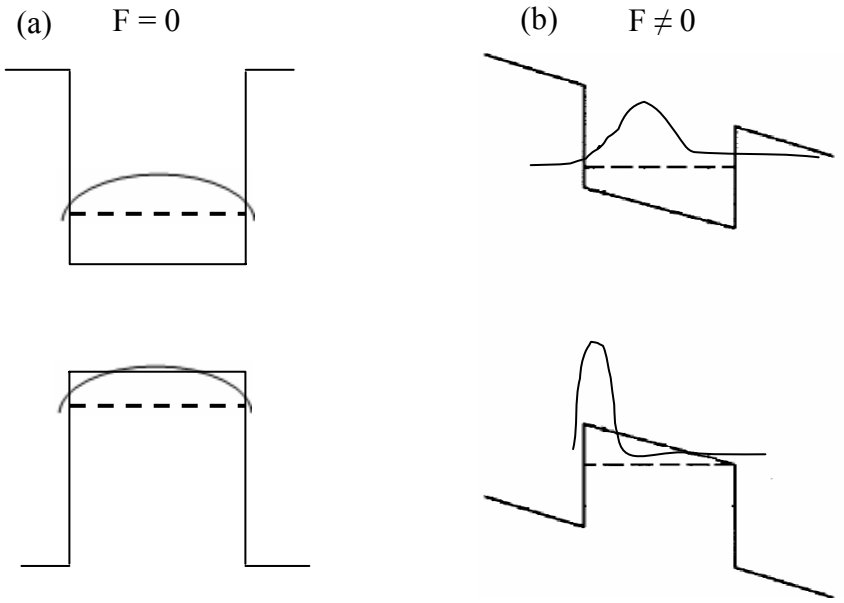

Fig. 1. (a) The wavefunction of electrons and holes in the absence of applied field, (b) effect of applied field pushes the electron and hole wavefunctions in the opposite direction.

Let us discuss theoretical analysis of the exciton resonance in the presence of a transverse electric field in quantum well structures. The Hamiltonian for this problem can be written as

$$H = H_{ez} + H_{hz} + H_{eh}$$

where each term in the right hand side can be expanded as,

$$H_{ez} = \frac{-\hbar^2}{2m^*_{e\perp}} \frac{\partial^2}{\partial z_e^2} + V_e(z_e) + eF_{z_e}$$

$$H_{hz} = \frac{-\hbar^2}{2m^*_{h\perp}} \frac{\partial^2}{\partial z_h^2} + V_h(z_h) - eF_{zh}$$

$$H_{eh} = \frac{-\hbar^2}{2\mu} \frac{\partial^2}{\partial r^2} - \frac{e^2}{4\pi\varepsilon\left[(z_e - z_h)^2 + r^2\right]^{1/2}}$$

where $V_e(z_e)$, $V_h(z_h)$ is the built in rectangular quantum well potential for electrons and holes due to the discontinuity in the conduction and valence band. z_e, z_h are the z-coordinate of the electron and hole. $m^*_{e\perp}$, $m^*_{h\perp}$ is the effective mass of the electrons and holes respectively in the z-direction, $\mu = m^*_{ell} m^*_{hll} / \left(m^*_{ell} + m^*_{hll}\right)$ is the reduced effective mass in the plane of the layers, and $\vec{r}$ is the relative position of electron and hole in the (x,y) plane. One can perform numerical analysis to calculate the exciton binding energy and the overall shift in the resonance peak.

An approximate solution can be found analytically by assuming temperature and carrier concentrations are low enough so that only the lowest subband for electrons and heavy holes are occupied. The applied d.c. electric field pushes the electrons to the left due to the electrostatic force and holes to the right. Thus, their wavefunctions becomes skewed. First-order time-independent non-degenerate perturbation method can be used to get distorted wavefunctions for both electrons and holes. Expanding the wavefunctions in a complete orthonormal set using unperturbed wavefunctions as the basis functions.

$$\phi_n = \sqrt{\frac{2}{W}} \sin\left(\frac{n\pi x}{W}\right) \quad \text{..... (1)}$$

$$\Psi_{distorted} = \sum_n c_n \Phi_n \quad \text{..... (2)}$$

where Φ_n is the unperturbed wavefunction, the distorted wavefunction can be expanded as

$$\Psi_{distorted} = \frac{c_1\Phi_1 + c_2\Phi_2 + c_3\Phi_3 + ...}{\sqrt{|c_1|^2 + |c_2|^2 + |c_3|^2 + ...}} \quad \text{..... (3)}$$

We can also calculate the co-efficients C_n

$$\frac{c_n}{c_1} = \frac{H'_{n1}}{(E_1 + H'_{11}) - (E_n + H'_{nn})}$$

where E is the electric field and H' is the perturbation term. The general expression for H'_{n1} is

$$H'_{n1} = \frac{2q\varepsilon}{W} \int_0^W \sin\left(\frac{n\pi x}{W}\right) \sin\left(\frac{\pi x}{W}\right) x dx \quad \text{..... (4)}$$

Evaluating the above equation, we get $H'_{n1}=0$ for n= 3, 5, 7… etc i.e. for all "odd" values of n. There is a physical explanation for this. We are trying to calculate the distorted wavefunction by mixing the subband wavefunctions in appropriate proportions, where C_n's are the weighting factors in this mixing, to get $\Psi_{distorted}$. Initially the wavefunction is symmetric and when a field is applied, the wavefunction becomes asymmetric. In order to

introduce asymmetry to the lowest subband wavefunction by mixing higher subband wavefunctions. One must introduce only wavefunctions for n= 2, n= 4 etc in the mixture, since their wavefunctions are asymmetric. The wavefunctions for odd values of n are symmetric. Consequently $C_3 = C_5 = \ldots 0$ for odd values of n and C_n is not zero for even values of n. Calculating all the C_n's and substituting in equation (3) we get the distorted wavefunction for electron and hole.

The strength of the radiative recombination is proportional to the overlap integral. The applied electric field decreases the overlap integral and correspondingly absorption or fluorescence strength. The overlap integral is

$$\int \Psi^{*}_{electron} \; \Psi_{hole} \, dx = \int \sum_{n} c^{e\,*}_{n} \, \phi^{*}_{n} \sum_{m} c^{h}_{m} \, \phi_{m} \, dx \quad \ldots\ldots\ldots\ldots\ldots\ldots (5)$$

Because of the orthogonality of the unperturbed wavefunctions, the above equation reduces to

$$\int \Psi^{*}_{electron} \; \Psi_{hole} \, dx = \sum_{m} c^{elec\,*}_{m} \; c^{hole}_{m} \quad \ldots\ldots\ldots\ldots\ldots\ldots\ldots\ldots\ldots\ldots\ldots\ldots (6)$$

Taking the modulus square of the above equation, we can get the absorption strength as a function of applied field.

Quantum confined stark effect due to built in charges

In heterostructures, large built in charges are very common and in some cases the built in field is large enough to cause Stark effect. Ref [6] reports giant Quantum Confined Stark Effect in AlGaN/GaN quantum well due to built in charges. In our samples, even without any externally applied electric field, there is still a built-in electric field transverse to the nanowire axis, possibly due to trapped charges in the alumina. These built in field tilts the conduction band and valence band edges causing a red-shift in the spectrum. Interestingly in the case of 25 nm ZnO wires sample, we saw the exciton peak being red-shifted by 15 nm. The figure below shows the tilt in the band edges due to built in charges that cause Stark effect.

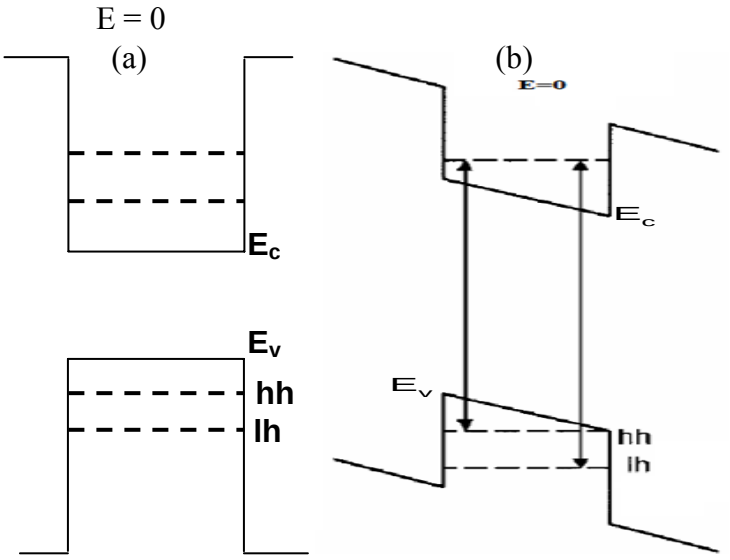

Fig. 2. (a) Band diagram of nanostructure with out built in charges (b) shows the tilt in the energy levels due to built in charges

This quantum confined stark effect in ZnO nanowires due to the built in charges will be discussed in detail in chapter 3 and chapter 2 will describe the steps involved in the

fabrication of ZnO and CdS nanowires. Chapter 4 discusses the giant exciton binding energy in CdS nanowires in the presence of dielectric de-confinement. Finally chapter 5 is the conclusion.

CHAPTER 2 FABRICATION OF HIGHLY ORDERED SEMICONDUCTOR NANOWIRES THROUGH ELECTROCHEMICAL SELFASSEMBLY METHOD

2.1 Introduction:

In this chapter, we describe the synthesis of nanowires using porous alumina template.

2.2 Electrochemical self-assembly

The basic steps involved in the fabrication of electrochemically self-assembled nanostructures using porous alumina technique are 1. Electropolishing, 2. Anodization and 3. Electrodeposition. The detail of the fabrication process is as follows.

2.2.1 Electropolishing

A 99.997 % pure commercially available Al foil (100 μm thick) is diced into 2cm by 2cm coupons. The coupons are then degreased in trichloroethane solution and washed thoroughly in D.I water. This is followed by electropolishing (using Electromet-4 Buehler Ltd) the Al foil in a solution consisting of 1050 cc ethyl alcohol, 150cc butyl cellosolve, 93cc perchloric acid and 205 cc of distilled water for various time duration and at various voltages. Electropolishing is carried out under dc condition with Al foil as the anode, in contact with the electrolyte. The optimum voltage and time to achieve regular ordered

patterns on the Al surface is reported in Ref [9]. A typical topographical AFM image of such electropolished coupons can be seen in the figure below

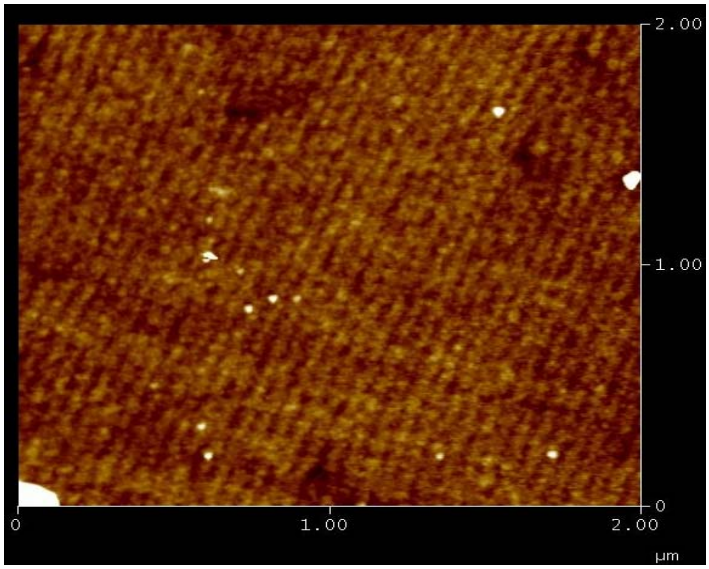

Fig. 3. Topographical AFM image of an electropolished Al coupons at 40V for 10 sec.

Fig 3 shows highly ordered patterns on the surface of the aluminum coupons and these patterns can be used as self-assembled masks for producing highly ordered arrays of nanostructures by mesa etching.

2.2.2 Anodization process

The electropolished samples are anodized under appropriate electrochemical conditions to get ordered pores of different diameter and lengths. In our lab, anodization is carried out using a Perkin-Elmer flat cell, in which a Pt mesh acts as the cathode and the electropolished aluminum foil acts as an anode. A dc voltage is applied across the two electrodes and a moderately strong acid is used as an electrolyte. A two-step anodization

process is employed to produce highly ordered pores on the Al surface. The top view AFM micrograph of a 50 nm pores is shown in Fig 7, where the dark areas correspond to pores and the surrounding light regions are alumina. Initial anodization is carried out for several hours to form a thick porous alumina film on the Al surface. This film is then stripped off in hot chromic/phosphoric acid. Anodization is repeated again for 5 minutes to form another porous alumina film of thickness less than 1 μm. Using this procedure, it is possible to get very well regimented array of pores over a large area of the sample. The schematic diagram showing complete experimental set-up for anodization is shown in Fig.4.

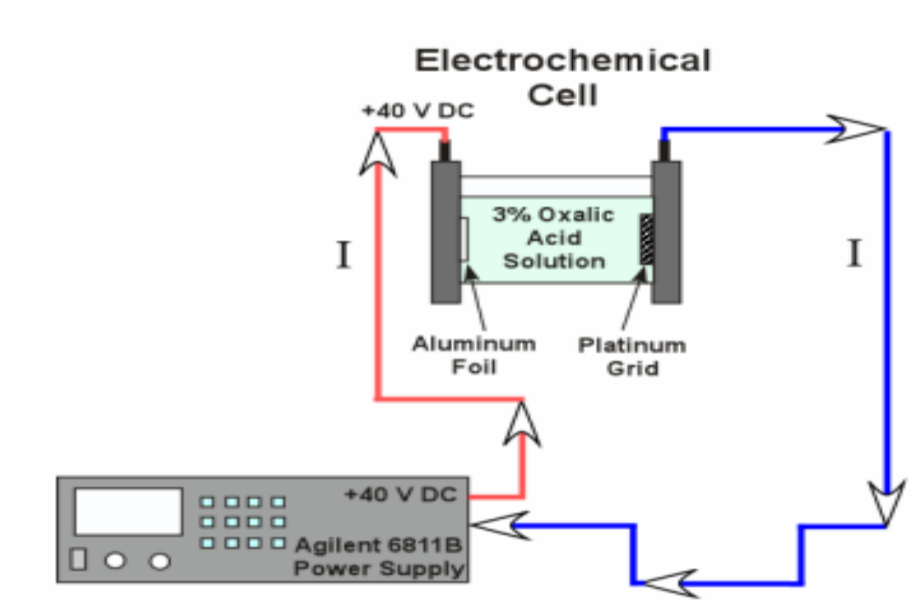

Fig 4. Schematic diagram of the complete experimental setup for anodization

A typical anodization current versus time curve is shown in Fig. 5. During the first few seconds of anodization the current falls rapidly until it reaches a minimum value. Beyond the minimum point, the current rises, goes up to a certain value and becomes constant.

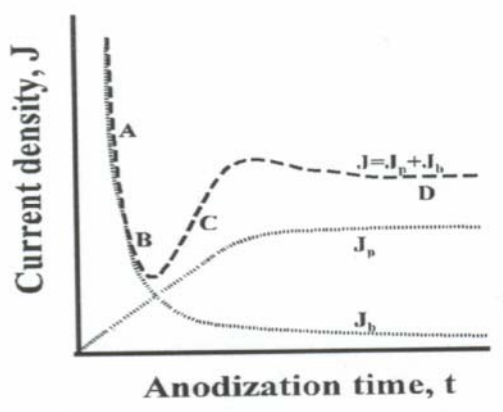

Fig 5. Variation of anodization current as a function of time

The above graph show the four stages involved in the pore formation as a function of time. When the voltage source is turned ON, an alumina barrier layer begins to form on Al surface. During this time, the current decreases as shown in Stage A of the above graph. Stage B corresponds to initiation of pores in the alumina layer. In stage C, pore growth continues and stage D corresponds to the steady state when the current becomes constant. The net current density "J" shown by the dotted line arises due to two different current components as shown in Fig. 5. One component, J_b, corresponds to growth of the barrier alumina, which decreases with time. The other component J_p, corresponding to pore-formation which increases with time. Thus, a competing mechanism of oxide growth and oxide dissolution, is responsible for the development of the final pore structure.

The chemical reactions taking place during pore formation is

$2Al + 3H_2O = Al_2O_3 + 6H^+ + 6e^-$ …… (1) at anode

$6H^+ + 6e^- = 3H_2$ …… (2) at cathode

$Al_2O_3 + 6H^+ = 2Al^{3+} + 3H_2O$ …… (3) dissolution of alumina

Figure 6 shows the schematic diagram of the pore structure in the final steady state. The pores grow perpendicular to the Al surface and parallel to each other. They are open at the top and closed at the bottom. There is a thin barrier layer of aluminum oxide present between the porous layer and the Al surface. The pore diameter, "*d*", inter-pore separation, "*D*" and pore lengths, "*L*" are controlled by fabrication conditions, in particular the acid used and the voltage applied during anodization.

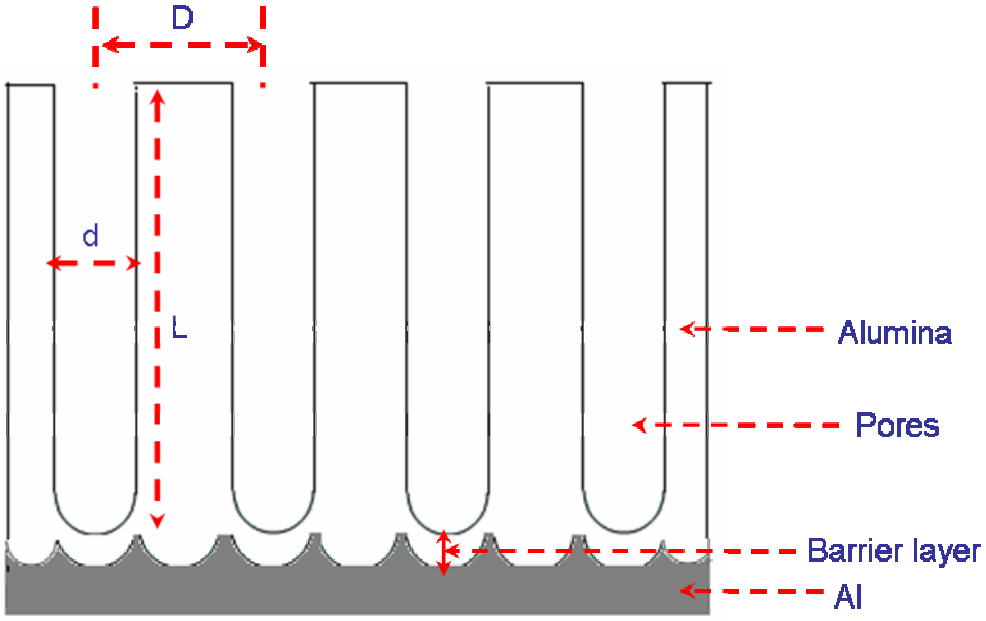

Fig. 6. Schematic diagram of the cross-section of a porous alumina template

Table [1] details the acids and voltages employed during anodization to get different pore diameters.

Pore diameter (nm)	Anodizing acid	Anodizing voltage (V dc)
50	3% oxalic	40
25	3% oxalic	25
10	15% sulfuric	10

Table 1 Describes the acids and voltages employed during anodization to get different pore diameters

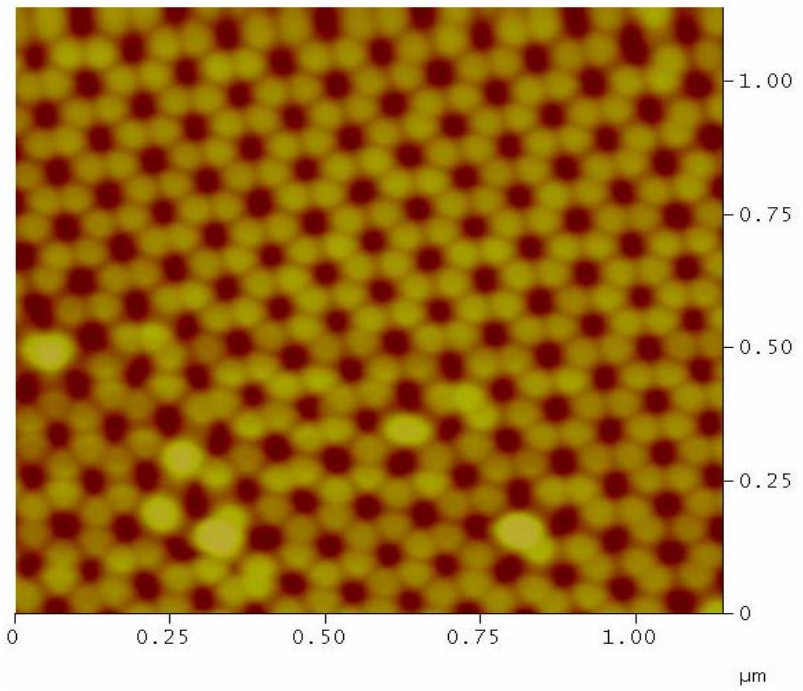

Fig 7 AFM image of the template with 50nm pores made using 3% Oxalic acid at 40V dc

2.2.3a Electrodeposition process

The nanoporous templates formed by anodization are selectively filled with the material of interest by electrodeposition process to get quantum dots or nanowires. At the end of the deposition, we get a two dimensional quasi-periodic arrays of vertically standing nanowires surrounded by alumina. The two types of electrodeposition methods followed in general are 1. AC electrodeposition, 2. DC electrodeposition. DC electrodeposition cannot be performed in the presence of insulating barrier layer. AC electrodeposition is one of the simple methods to fabricate quantum dots or nanowires inside nanoporous alumina template without removing the barrier layer. The details of the ac electrodeposition will be discussed in the next section.

2.2.3b Deposition of CdS and ZnO nanowires

A Perkin Elmer flat cell is used for electrodeposition process, in which a Pt mesh acts as the cathode and porous alumina film acts as the anode. The electrolyte contains non-aqueous solution of the metal bearing salt that is to be deposited selectively inside the pores. CdS is electrodeposited inside the porous alumina film in an electrolyte consisting of 10.5 g of cadmium perchlorate, 2.5 g of lithium perchlorate and 1 g of sulfur powder dissolved in 250 ml of dimethyl sulfoxide. In the case of ZnO, cadmium perchlorate is replaced by zinc perchlorate. The electrolyte is heated to 90^{o} C and then electrodeposition is carried out by applying 25 V AC at a frequency of 250 Hz for few minutes. During negative half cycles, Cd^{++} or Zn^{++} ions gets deposited at the bottom of the pores, since the bottom of the pores offer least resistance path for the current to flow and then these ions

are reduced to zero valent Cd or Zn. During the positive half cycles Cd or Zn will not be re-oxidized due to the *valve metal oxide* nature of anodic alumina, which conducts current preferentially only in one direction namely anodic half cycles. At high temperature of the solution, sulfur atoms in the solution react with Cd to form CdS inside the pores. In order to produce ZnO, metallic Zn is deposited inside the pores. Once the metallic Zn nanowires are formed, the sample is washed thoroughly in D.I water, dried and then immersed in hydrogen peroxide solution for 6~8 hours to oxidize the metallic Zn to form ZnO nanowires. The Fig 8 and 9 shows the plot of current versus the deposition time for 50 nm zinc oxide and cadmium sulfide nanowires.

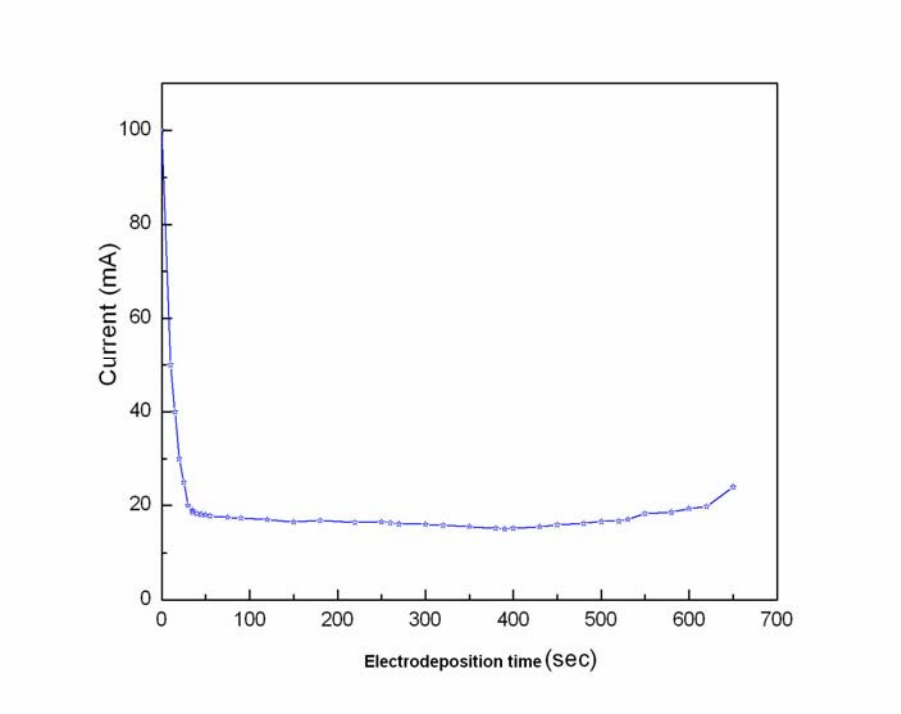

Fig. 8. Current Vs electrodeposition time of 50 nm CdS nanowires

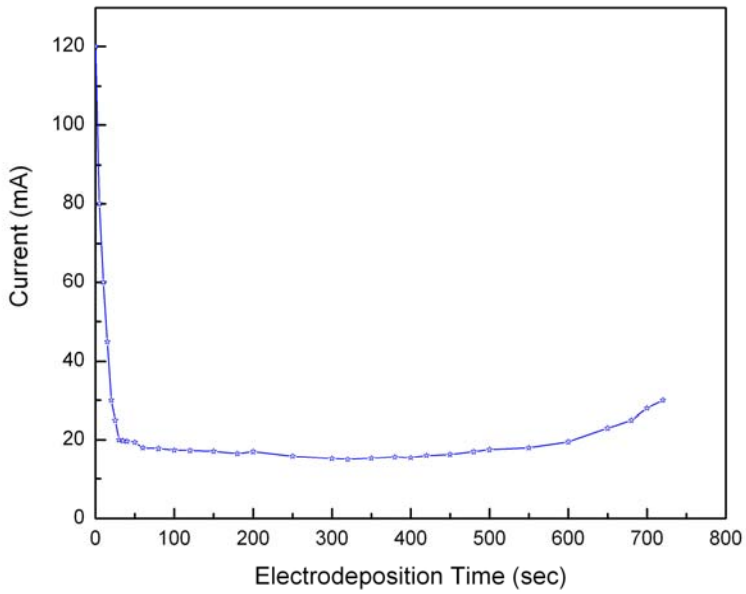

Fig. 9. Current Vs electrodeposition time of 50 nm ZnO nanowire

The nanowire lengths can be controlled by monitoring the deposition currents. During the initial stage of deposition, current decreases rapidly, reaches a minimum value, and stabilizes after few seconds, indicating a steady deposition of the material inside the pores. Once the pore is filled to the brim, we can see a sharp rise in the current. Typically, the deposition is carried out until this time. The samples are then rinsed thoroughly in D.I. water and made ready for characterization.

2.4 TEM Characterization of nanowires

In order to carry out TEM imaging, the semiconductor nanowires have to be released from the alumina host. It is done by soaking the sample in hot chromic phosphoric acid, which

dissolves alumina and the wires are released in the acid. The released wires will not react with hot chromic phosphoric acid. The acid containing the wires is collected in a centrifuge tube and centrifugation is performed. After centrifugation, the wires are collected at the bottom of the tube and excess acid is removed from the tube. This process is repeated until all the acid is removed and finally ethyl alcohol is added. Ultrasonication is carried out to release the wire from the bottom of the tube. The dispersed wires are captured in a formwar polymer coated TEM grid and imaging is carried out. TEM image of an isolated 50 nm ZnO nanowire is shown below

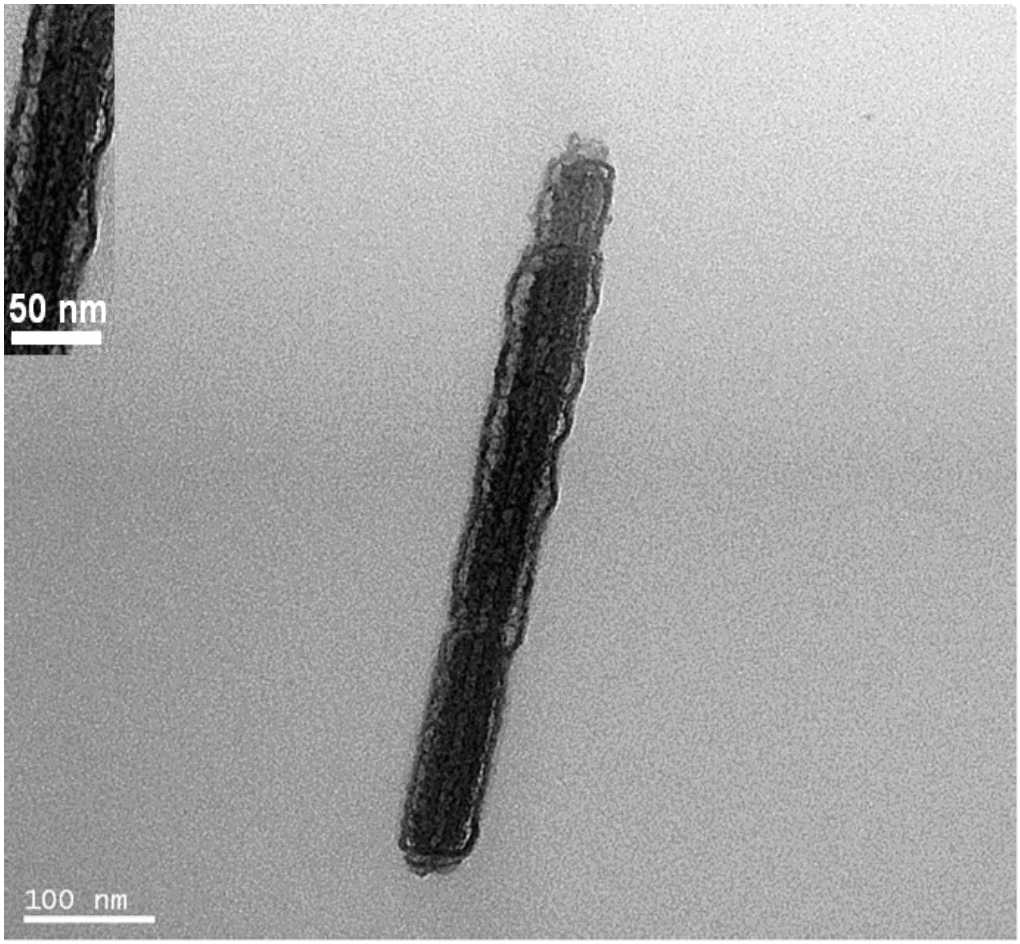

Fig 11. Transmission electron micrograph of an isolated zinc oxide nanowire

CHAPTER 3 ROOM TEMPERATURE FLOUROSCENCE AND FTIR SPECTROSCOPY CHARACTERIZATION OF ZINC OXIDE NANOWIRES: EVIDENCE OF QUANTUM CONFINED STARK EFFECT[1]

3.1 Introduction

Semiconductor nanowires offer unique electrical and optical properties and have been a subject of active research over the last few decades. ZnO is a wide band gap semiconductor with a band gap of 3.37 eV and is therefore a suitable material for ultraviolet lasers. Compared to other wide band gap materials, it has high exciton binding energy (60meV), which is sufficient to achieve exitonic laser action at room temperature, since the binding energy is greater than the thermal energy k_BT (= 25meV at room temperature). Many research groups have been able to successfully fabricate ZnO nanowires and nanorods by a variety of techniques [16-23]. In this work, we have fabricated ZnO nanowires through electrochemical self-assembly method and carried out fluorescence spectroscopy characterization to study the exciton features, binding energy, trap state emission etc. Fluorescence spectra also shows strong evidence of quantum confined Stark effect, where by the fluorescence spectra can be modulated by external applied potential. This can lead to inexpensive electro optic devices and wavelength tunable ultra violet laser [1-5].

[1] This part of the work is published in Journal of Material Science: Materials in Electronics

3.2 Fluorescence spectroscopy

In fluorescence spectroscopy, one measure physical properties of the material by shining photons to excite electrons to higher energy levels and analyzing the optical emission as these states relax. The spectral distributions of the emission are related to electronic transition probabilities with in the sample. It can provide quantitative information like exciton transition, exciton binding energy, trap states, impurities states etc. The schematic diagram below shows the optical excitation in nanostructures

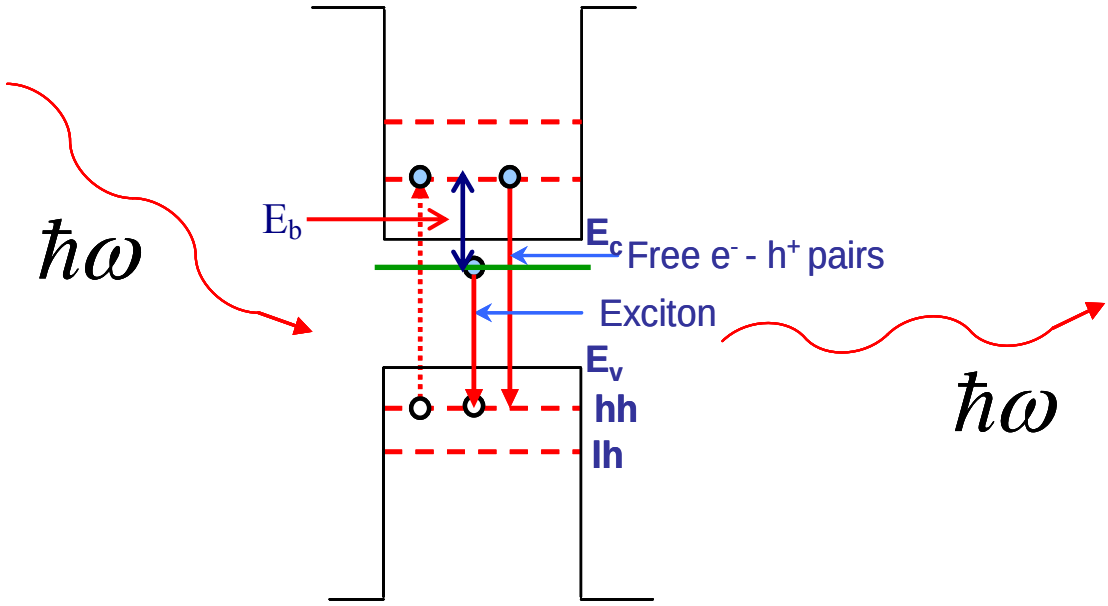

Fig. 12. Optical excitation in Nanostructures

3.2.1 Fluorescence spectroscopy of ZnO nanowires

We have used JY Horiba Fluoromax-3, Fluorolog Tau-3 spectrometer and Xenon arc lamp to excite the samples. The sample is excited at 290nm wavelength at room temperature.

The emitted photons are captured using standard single photon detector tube. The excitation photon energy is greater than the bandgap energy of ZnO (E_g =3.37 eV), so that electrons in the valence band will have sufficient energy to reach the higher energy levels and decay to the ground state and recombine radiatively. The wavelength Vs FL intensity plot is recorded and digitally stored in computer. Figure 14 shows the spectra recorded for 10, 25, 50 nm ZnO nanowires

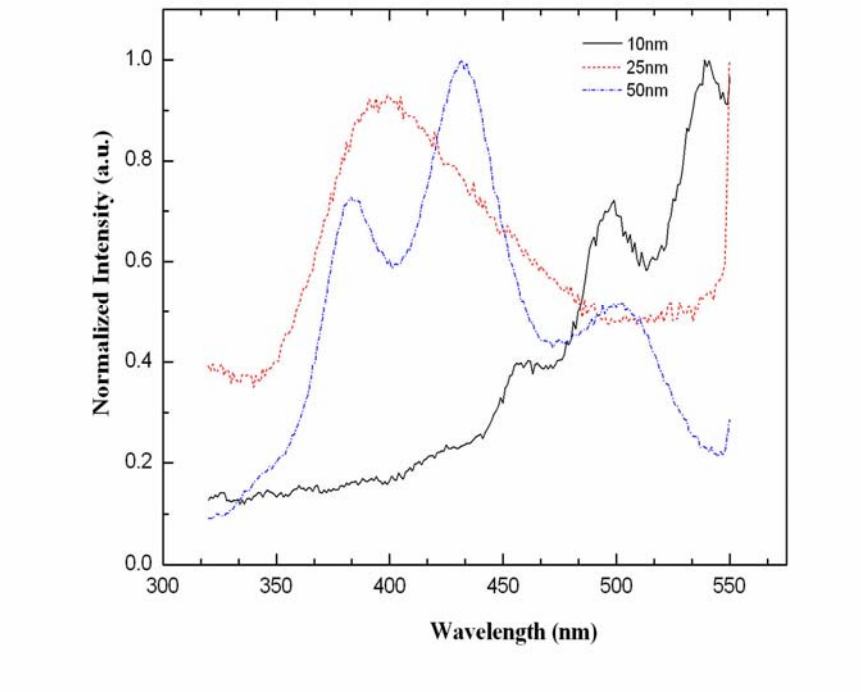

Fig 14. Fluorescence spectra of three different ZnO diameter nanowires recorded at room temperature.

3.2.2 Results and Discussion of FL spectra of ZnO nanowires

The fluorescence spectrum shows different peaks for different ZnO nanowires diameter. The spectra typically consist of two bands: a low frequency (green) band associated with

emissions from deep levels induced by structural defects, and a high frequency (ultra-violet) band associated with bound exciton recombination[6, 25-28].

10-nm diameter wires did not show any high frequency peak, but shows a low frequency peak centered at 490 nm wavelength. This emission is due to deep trap levels present in nanowires. This result is consistent with report found in Ref. [16]. This group also failed to observe the high frequency peak in 20-nm diameter wires produced in alumina templates, and observed only low frequency peak emission around the same wavelength.

The 25-nm diameter wires show the high frequency peak centered at a wavelength of 390 nm. The full-width-at-half-maximum (FWHM) linewidth is about 430 meV which is much larger than the thermal energy kT. Therefore, this linewidth is clearly the result of inhomogeneous broadening accruing from variations in the length of the nanowires. We did not see low frequency peak emission in 25 nm wire diameter.

Finally 50-nm diameter wires show both the high- and the low-frequency peaks. The spectra for 50 nm wires show many peaks related to different emission mechanisms. A peak centered at 380 nm, which corresponds to the exciton recombination peak of ZnO, while a 430 nm peak has been associated to oxygen vacancies (F^+ centers) in alumina templates [29-30] and its origin has been confirmed by electron paramagnetic resonance measurements [31]. In addition we found a peak at 515 nm due to the trap levels present in nanowire.

Comparing the three different spectra we can conclude that there is an evidence of Quantum Confined Stark Effect (QCSE) in the emission spectra of 25 nm wires. Here the exciton peak is red shifted by 15 nm, which can only happen via stark effect. QCSE can be present in our porous alumina samples, because there are strong built-in electric fields in the alumina templates due to trapped charges [32, 33]. These fields induce the quantum confined Stark effect [6, 32] which tends to quench the high frequency peak associated with exciton recombination and also induces a red shift in the peak position. The red shift comes about because the built in charges in the alumina tilts the energy levels and correspondingly shifts the absorption peak position. This in turn induces red shift in the emission wavelength.

The band gap of ZnO is 3.37 eV and the exciton binding energy is 60 meV [35, 36]. Therefore, we expect the high frequency peak to be centered at an energy of 3.37 – 0.06 = 3.31 eV, or a wavelength of 375 nm, if we neglect any blue shift caused by quantum confinement. In the 50-nm sample a peak seen around this value, but in the 25-nm sample, the peak is centered at around 390 nm. It means that there is at least a 15 nm red-shift. This is a surprising result and counter-intuitive. We actually expect the emission peak in the 25-nm sample to be blue-shifted compared to the 50-nm sample, because of stronger quantum confinement. Yet we consistently observe the opposite trend. This can be explained by either strain effects or the quantum confined Stark effect. Strain effects are negligible since the nanowires are not single crystals (they are polycrystalline). Therefore, the likely cause is the quantum confined Stark effect which renormalizes the subband energies in a

nanowire and induces a red-shift in the emission peak. Note that the actual red-shift in the 25-nm sample is probably *larger* than 15 nm, since we did not account for any blue-shifts caused by quantum confinement. In the case of 10 nm samples the electric field due to built in charges is very high, which completely quenches the high frequency peak that is probably why we do not see it. In the spectra we also saw emission due to deep levels present in the nanowires. The figure below shows the build in charges present in the porous alumina matrix. These charges are mostly due to interface states. In the case of CdS nanowire, the interface state density is about $2 \times 10^{13}/cm^2$ [45].

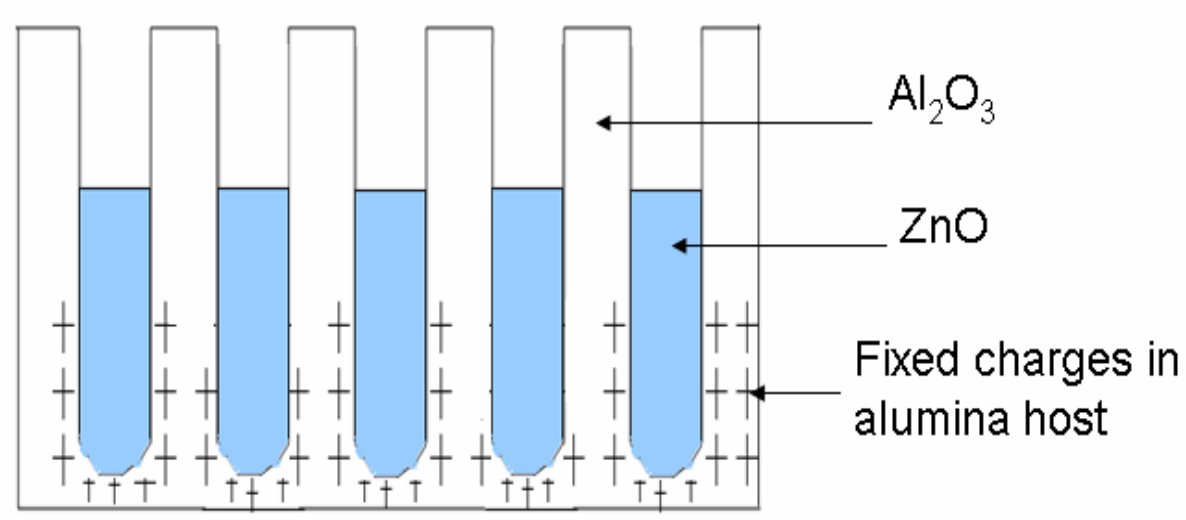

Fig. 15. Built in charges present in the porous alumina template

Every observed feature is consistent with the quantum confined Stark effect. The built-in electric fields are likely to be progressively larger in anodic alumina films with smaller pores because the "porosity" (defined as the ratio of pore volume to the volume of

alumina) decreases with decreasing pore diameter. Thus, samples with smaller pores have more alumina available in a given volume to host more fixed charges, and therefore a larger built-in electric field. Accordingly, the 10-nm samples have the largest built-in electric fields, which ionize the excitons and completely quench the high frequency peak associated with exciton recombination. That is why we do not observe the high frequency peak in these samples. The 25-nm samples have intermediate values of built-in fields, which are not strong enough to quench the high frequency peak completely, but induce a red shift of at least 15 nm. Finally, the 50-nm samples have the weakest built-in fields. Therefore, the high frequency peak is least affected in these samples, both in terms of intensity and frequency shift.

3.3 FTIR absorption measurements of ZnO nanowires

In addition to UV characterization, we have also carried out IR characterization to shed light on impurity states in the nanowires. An ABB BOMEM spectrometer is used to carry out Fourier transform infrared (FTIR) spectroscopy. The infrared absorption spectrum of ZnO nanowires is taken at room temperature. The IR absorption spectrum of 10-, 25- and 50-nm diameter wires is shown below. These spectra are obtained after subtracting the spectra of the bare anodic alumina membrane from the total absorption spectra. We see no peaks (the ripples are due to interference effects caused by the finite thickness of the membranes) in the near infrared region, indicating that there are no shallow level traps. There is a weak peak in the long wavelength region (centered at a wavelength of 13.3 μm)

that appears in the 25-nm samples. The transition energy associated with this peak is 92 meV. Since the effective mass of electrons in the conduction band is 0.27 times the free electron mass [36], the energy separation between subbands in the conduction band is ~ 6.6 meV for quantum dots with dimensions of 25-nm on the edge (assuming hard-wall boundary conditions and a square well potential). Even if we account for side depletion due to interface states, which is known to reduce the effective carrier confinement volume in these nanostructures [37, 9], we cannot explain the large transition energy of 92 meV by ascribing it to inter-subband excitation. Therefore, this peak is most likely caused by carrier transfer from unintentional dopants producing impurity levels near the conduction band edge.

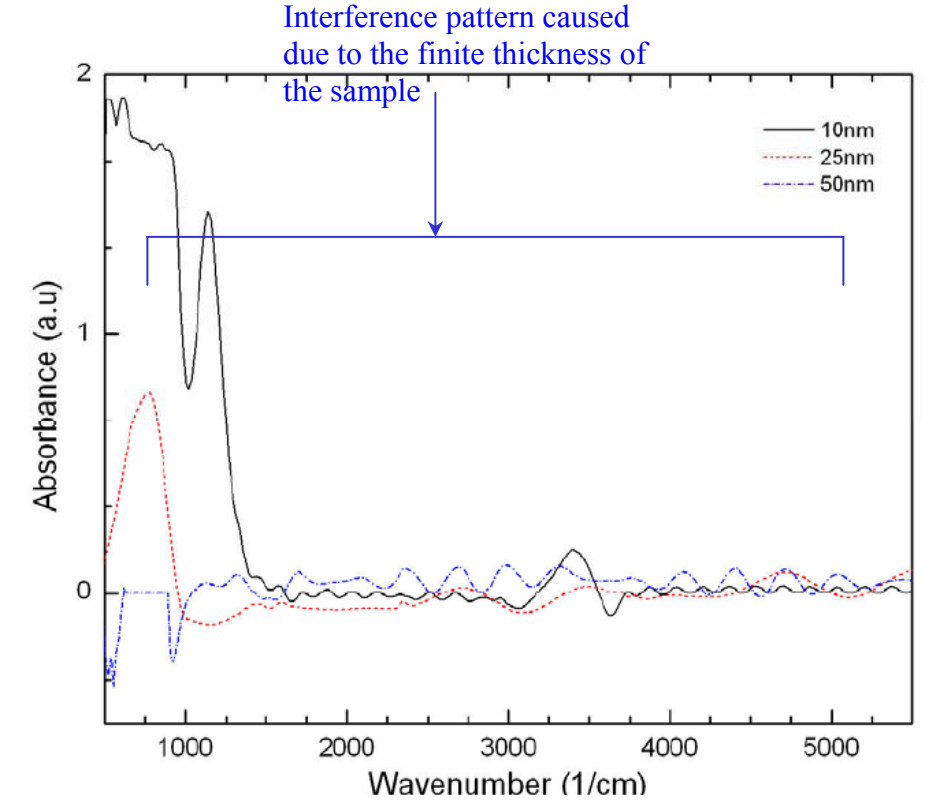

Fig. 16. Room temperature FTIR absorption spectrum for three different ZnO nanowires diameters

Chapter 4 GIANT EXCITON BINDING ENERGY IN SEMICONDUCTOR NANOWIRES IN THE PRESENCE OF DIELECTRIC DECONFINEMENT [2]

4.1 Introduction

In a semiconductor nanowires (or "quantum wire"), photoexcited electrons and holes are free to move along the length of the wire, but their motion is restricted along the other two transverse directions. That results in a large overlap between the electron and hole wavefunctions, which increases the binding energy of the excitons. The increase is significant if the wire radius is comparable to or smaller than the exciton Bohr radius. As a result, excitonic transitions dominate the absorption and luminescence (or fluorescence) spectra. In addition to quantum confinement effect, exciton binding energy can be influenced depending upon the material surrounding the semiconductor wire. If the insulator has a *smaller* dielectric constant compared to semiconductor, then the exciton binding energy is increased [38-40]. This is known as "*dielectric confinement*" or "*dielectric enhancement*" effect. On the other hand, if the insulator has a *larger* dielectric constant, then the binding energy is reduced. This effect is called "*dielectric de-confinement effect*". In the case of "*confinement*", the electric field lines connecting the electron and hole pairs reside mostly with in the semiconductor, which increases the exciton binding energy. In the case of "*de-confinement*", the opposite happens.

[2] This part of the work has been published in the Proceedings of 6th IEEE conference on Nanotechnology (IEEE-Nano), Cincinnati, 2006

4.2 Room temperature fluorescence spectroscopy of CdS nanowires

In this study three different CdS wire diameters say 10-, 25-, 50 nm are characterized at room temperature. The sample is excited at 425 nm using a xenon arc lamp, whose photon energy is greater than the band gap energy of the semiconductor. The emitted photons are captured by a photo-detector tube and results are stored digitally. The figure below shows the resulting fluorescence spectra

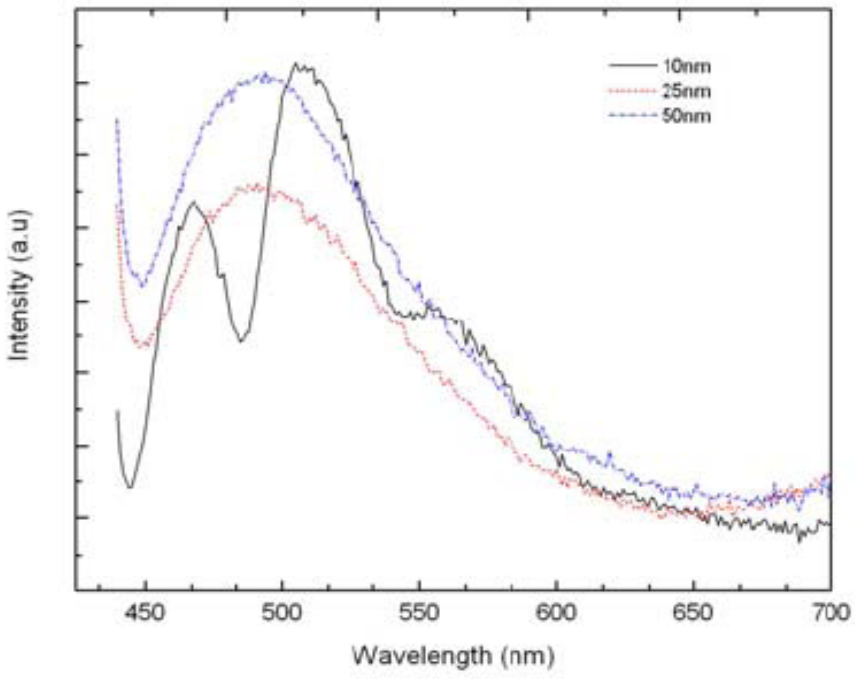

Fig. 18. Room temperature fluorescence spectra of 10, 25, 50 nm CdS nanowires

The 25 and 50 nm spectra looks similar with broad peak of 300 meV (FWHM). The 50 nm peak is centered at 495 nm and 25 nm peak is centered at 490nm. The corresponding photon energies are 2.50 eV and 2.53 eV respectively. In the case of 25 nm wires, there is a

blue shift of 30 meV due to the quantum confinement which increases the effective bandgap. The bulk bandgap of CdS is 2.50 eV [36], so we can assign these peaks to radiative recombination of free electron-hole pairs. The peak width of 300 meV is due to inhomogeneous broadening. There is significant variation in the length of the nanowires, which causes this width. The diameters of the wires deviate by less than 10% from the average value, but the length can vary over an order of magnitude.

In the case of 10nm wire, the spectra show interestingly two peaks. The low frequency peak is centered at 510 nm and high frequency centered at 467nm. The corresponding photon energies are 2.43 eV and 2.65 eV. The low frequency peak cannot be due to free electron-hole recombination since the photon energy is less than the band gap of the semiconductor. So it must be related to bound electron-hole pair recombination. In other words, it is called exciton peak. The high frequency peak is due to radiative recombination of free electron-hole pairs. The 10nm sample shows a peak which is blueshifted by 150 meV due to quantum confinement. We can calculate the exciton binding energy for 10nm wires from the two peak positions. It is given by

$$E_b = 2.65\ eV - 2.43\ eV = 220\ meV$$

The exciton binding energy in bulk CdS is 28 meV [41], which makes it difficult to observe the exciton peak at room temperature. In 10-nm diameter wires, the binding energy has gone up to 220 meV, which makes the exciton peak observable at room temperature. We also notice that the line width is reduced to ~ 140 meV in the 10-nm wires, indicating that the smaller diameter wires have a smaller dispersion in the length and

less surface states are involved. Ref. [40] measured the photoluminescence spectrum of 10-nm CdS wires in an anodic alumina matrix and found very similar behavior. They too observed a large increase in the exciton binding energy and reported it as 170 meV, which is somewhat smaller than what we find.

Based on the blue shift obtained we can calculate the effective wire radius of the sample. We know that due to side depletion caused by the interface states decreases the effective radius of wire significantly. From the measured blue shift, effective confining radius of the exciton can be estimated using a hard wall potential model.

Physical wire radius (nm)	Effective wire radius (nm)
25	4
12.5	3.4
5	2.3

Table [2] Effective wire radius calculated for different physical wire radius

Ref [9, 37] reports the effective wire diameter for 10 nm CdS wires to be 3.5 nm due to side depletion caused by interface states, above table shows the effective diameter ~ 4.6 nm which is quite reasonable. We do not observe the exciton peak in the 25- and 50-nm samples. These could be due to the fact that in these samples the exciton binding energy is too small, less than the thermal energy kT, so that the excitons are thermally ionized at room temperature. The other possibility is that the broad line width of the free carrier

recombination peak masks the exciton peak. Strong quantum confinement in the 10-nm wires not only increases the exciton binding energy, but it also increases the oscillator strength associated with exciton recombination, thereby making the exciton peak dominant over the free carrier recombination peak. That feature adds to the "visibility" of this peak.

4.2.1 Dielectric De-confinement effect

The quantum confinement increases the exciton binding and oscillator strength and it can be further enhanced or decreased depending upon the relative permittivity of the material surrounding the semiconductor wire. If the semiconductor is surrounded by an insulating material of higher dielectric constant then the oscillator strength is decreased which in turn decreases the exciton binding energy. This allows one to change the binding energy and oscillator strength over a wide range of values by varying the permittivities of semiconductor and insulator and thus realizing "*Coulomb interaction engineering*". Ref. [40] erroneously attributed some of the increase in the exciton binding energy due to the dielectric confinement effect based on their assumption that the dielectric constant of alumina (an insulator) is less than that of CdS (a semiconductor). In reality, alumina has a higher dielectric constant than CdS. The relative dielectric constant of CdS is 5.4 [36]. There is some dispersion in the value of the relative dielectric constant reported for alumina. Ref. [42] reports it to be as low as 8.0 while ref. [43] reports it as 9.75. However, this entire range of values is larger than 5.4. Ref. [44] claims that they have achieved a low relative dielectric constant of 2.4 in porous anodic alumina. Only at optical frequencies the

dielectric constant can be as low as 2~4, which is not relevant to our case. In our case, dc relative dielectric constant is relevant because the electric field lines connecting electrons and holes is purely *"DC"* in nature and does not change with time.

Because the alumina has a larger dielectric constant, the electric field lines connecting the electron and hole in an exciton reside mostly in the alumina. This *decreases* the exciton binding energy owing to the dielectric de-confinement effect. In spite of that, we observe an 8-fold increase in the binding energy of exciton in 10-nm diameter wires from its bulk value. This must come entirely from quantum confinement. We note that the exciton Bohr radius in bulk CdS is ~ 5 nm, while the effective wire radius is ~ 2.3 nm if we take side depletion into account. Therefore, the exciton Bohr radius is squeezed inside the potential well causing an eight fold increase in the binding energy. In this case quantum confinement effect far outweighs the dielectric de-confinement effect causing a giant increase in exciton binding energy.

Chapter 5 Conclusions

We have shown a simple and inexpensive way to fabricate ZnO and CdS nanowires through electrochemical self-assembly technique. The fabrication steps involved is very easy and has rapid throughput. These structures are ideal to carry out transport, magnetic and optical studies.

Fluorescence spectroscopy of ZnO nanowires reveals a strong evidence for Quantum confined Stark effect, which can be used to modulate the emission frequency with an externally applied electrostatic potential [1]. This can lead to inexpensive wavelength-tunable ultra-violet lasers and electro-optic devices.

Fluorescence spectroscopy of 10 nm CdS nanowires exhibited giant exciton binding energy (220 meV) in the presence of dielectric de-confinement effect. Based on the fluorescence spectra obtained for three different CdS nanowires, we conclude that when exciton Bohr radius > 2 × the effective nanowires radius, then quantum confinement effect far outweighs the dielectric de-confinement effect giving raise to giant exciton binding energy. The strong increase in exciton binding energy can be exploited to realize inexpensive room temperature luminescent devices.

LIST OF REFERENCES

List of references

[1]. D.A.B Miller, D.S. Chemla, T.C. Damen, A.C. Gossard, W. Wiegmann, T.H. Wood, C.A. Burrus, *Physical Review Letters*, Vol **53**, (1984), 2173

[2]. D.A.B. Miller, D.S. Chemla, S. Schmitt-Rink, *Phys Rev B*, Vol **33**, (1986), 6976

[3]. D.A.B. Miller, Joseph S. Weiner, D.S. Chemla, *IEEE Journal of Quantum Electronics*, Vol **9**, (1986), 1816

[4]. Leo Esaki, *IEEE Journal of Quantum Electronics*, Vol **9**, (1986), 1611

[5]. R.K. Gug, W.E. Hagston, *Journal of Applied Physics*, Vol **86**, (1999), 5012

[6]. N. Grandjean, B. Damilano, S. Dalmasso, M. Leroux, M. Laugt, J. Massies, *Journal of Applied Physics*, Vol **86**, (1999), 3714

[7]. H. Masuda and K. Fukuda, *Science*, Vol **268**, (1995), 1466

[8]. *Quantum Dots and Nanowires*, Edited by Supriyo Bandyopadhyay, Hari Singh Nalwa**,** *chapter four*, Synthesis of Nanowires Using Porous Alumina, Latika Menon, additional references in that article

[9]. S. Bandyopadhyay, A E Miller, H C Chang, G Banerjee, V Yuzhakov, D-F Yue, R E Ricker, S Jones, J A Eastman, E Baugher, M Chandrasekhar, *Nanotechnology*, **7**, (1996), 360.

[10]. C-G Stefanita, S. Pramanik, A. Banerjee, M. Sievert, A. A. Baski and S. Bandyopadhyay, *J. Crystl. Growth*, **268**, (2004), 342

[11]. E. M. Wong and P. C. Searson, *Appl. Phys. Lett.*, **74**, (1999), 2939

[12]. B. Sang and M. Konagai, *Jpn. J. Appl. Phys.*, Pt. 2, **35**, (1996), L602.

[13]. H. Nanto, T. Minami and S. J. Takata, *J. Appl. Phys.*, **60**, (1986), 482.

[14]. A. V. Nurmikko and R. L. Gunshor, *Solid St. Commun.*, **92**, (1994), 113.

[15]. X-L Guo, J-H Choi, H. Tabata and T. Kawai, *Jpn. J. Appl. Phys.*, Pt. 2, **40**, (2001), L177.

[16]. Y. Li, G. W. Meng, L. D. Zhang and F. Phillipp, *Appl. Phys. Lett.*, **76**, (2000), 2011.

[17]. Seu Yi Li, Chia Ying Lee, Pamg Lin and Tseung Yuen Tseng, *J. Vac. Sci. Technol. B*, **24**, (2006), 147.

[18]. Shingo Hirano, Nobuo Takeuchi, Shu Shimada, Kyosuke Masuya, Katsuhiko Ibe, Hideo Tsunakawa, and Makut Kuwabara, *J. Appl. Phys.*, **98**, (2005), 094305.

[19]. Yanfeng Zhang, Richard E. Russo and Samuel S. Mao, *Appl. Phys. Lett.*, **87**, (2005), 043106.

[20]. Zhiyong Fan and Jia G. Liu, *Appl. Phys. Lett.*, **86**, (2005), 123510.

[21]. Zhiyong Fan, Pai-chun Chang, Jia G. Lu, Erich C. Walter, Reginald M. Penner, Chien-hung Lin and Henry P. Lee, *Appl. Phys. Lett.*, **85**, (2004), 6128.

[22]. Y. W. Heo, L. C. Tien, Y. Kwon, D. P. Norton, S. J. Pearton, B. S. Kang and F. Ren, *Appl. Phys. Lett.,* **85**, (2004), 2274.

[24]. H. Masuda and M. Satoh, *Jpn. J. Appl. Phys.*, Pt. 1, **35**, (1996), 1126.

[25]. Qingtao Wang, Guanzhong Wang, Bo Xu, Jiansheng Jie, Xinhai Han, Gongpu Li, Qingshan Li and J. G. Hou, *Materials Letters*, **59**, (2005), 1378.

[26]. H. Bethke, H. Pan and B. W. Wessels, *Appl. Phys. Lett.*, **52**, (1988), 138.

[27]. Yang Zhang, Bixia Lin, Xiankai Sun and Zhuxi Fu, *Appl. Phys. Lett.*, **86**, (2005), 13190.

[28]. Z. W. Liu, C. K. Ong, T. Yu and Z. X. Shen, *Appl. Phys. Lett.*, **88**, (2006), 053110.

[29]. Y. Yamamoto, N. Baba and S. Tajima, *Nature (London)*, **289**, (1981), 572.

[30]. Y. Du, W. L. Cai, C. M. Mo, J. Chen, L. D. Zhang and X. G. Zhu, *Appl. Phys. Lett.*, **74**, (1999), 2951.

[31]. K. Vanheusden, W. L. Warren, C. H. Seager, D. K. Tallant, J. A. Voigt and B. E. Gnade, *J. Appl. Phys.*, **79**, (1996), 7983.

[32]. Y. Wang, S. Ramanathan, Q. Fan, F. Yun, H. Morkoc and S. Bandyopadhyay, *J. Nanosci. Nanotech*, Vol **6**, (2006), 2077

[33]. S. Sarkar, et al. (pre-print).

[34]. J. S. Jie, G. Z. Wang, Q. T. Wang, Y. M. Chen, X. H. Han, X. P. Wang and J. G. Hou, *J. Phys. Chem. B*, **108**, (2004), 11976.

[35]. J. C. Johnson, K. P. Knutsen, H. Q. Yan, M. Law, Y. F. Zhang, P. D. Wang and R. J. Saykally, *Nano Lett.*, **4**, (2004), 197.

[36]. S. M. Sze, *Physics of Semiconductor Devices*, 2nd edition (John Wiley & Sons, New York, 1981).

[37]. A. Balandin, K. L. Wang, N. Kouklin and S. Bandyopadhyay, *Appl. Phys. Lett*., **76**, (2000), 137.

[38]. L. V. Keldysh, *Phys. Stat. Solidi (a)*, **164**, (1997), 3.

[39]. V. S. Dneprovskii, E. A. Zhukov, E. A. Muljarov, and S. G. Tikhodeev, *JETP*, **87**, (1998), 382.

[40]. V. Dneprovskii, S. Gavrilov, E. Muljarov, A. Syrnicov and E. Zhukov, "Optical properties of CdS nanostructures crystallized in the pores of insulating template", *Proc. 9th Int. Symp. Nanostructures: Physics and Technology, St. Petersburg, Russia, June 18-22 (2001)*; S. A. Gavrilov, V. V. Gusev, V. S. Dneprovskii, E. A. Zhukov, A. N. Syrnikov, I. V. Yaminskii and E. A. Muljarov, *JETP Lett.*, **70**, (1999), 216.

[41]. *Excitonic Processes in Solids*, edited by M. Ueda, H. Kanzaki, K. Kobayashi, Y. Toyozawa and E. Hanamura, Springer Series in Solid State Sciences, Vol. **60** (Springer, Berlin, 1986).

[42]. L. L. Young, *Anodic Oxide Films* (Academic, New York, 1971)

[43]. William E. Courtney, *IEEE Trans. Microwave Theory and Techniques*, MTT-18, (1970), 476.

[44]. Porous alumina as a low−ε insulator for multilevel metallization", *Microelectron. Engr*., **50**, (2000), 321.

[45]. V. Pokalyakin, S. Tereshin, A. Varfolomeev, D. Zaretsky, A. Baranov, A. Banerjee, Y. Wang, S. Ramanathan and S. Bandyopadhyay, J. Appl. Phys. **97**, (2005), 124306

[46]. Jasprit Singh, Semiconductor Optoelectronics, 1st edition, (Mc.Graw-Hill, Newyork, 1995)

[47]. Peter Y. YU, Manuel Cardona, *Fundamentals of semiconductors*, 2nd edition, (Springer, Germany, 1999)